

New multi-zoom method for N-body simulations: application to galaxy growth by accretion.

B. Semelin¹ and F. Combes¹

Observatoire de Paris, LERMA, 61 Av. de l'Observatoire, F-75014, Paris, France

Abstract. The growth of galaxies is driven by two processes: mergers with other galaxies and smooth accretion of intergalactic gas. The relative share of these two processes depends on the environment (rich cluster or field), and determines the morphological evolution of the galaxy. In this work we focus on the properties of accretion onto galaxies. Through numerical simulations we investigate the geometrical properties of accretion. To span the scale range required in these simulations we have developed a new numerical technique: the *multi-zoom method*. We run a series of Tree-SPH simulations in smaller and smaller boxes at higher and higher mass resolution, using data recorded at the previous level to account for the matter inflow and the tidal field from outside matter. The code is parallelized using OpenMP. We present a validation test to evaluate the robustness of the method: the pancake collapse.

We apply this new *multizoom method* to study the accretion properties. Zooming in onto galaxies from a cosmological simulation, we select a sample of 10 well resolved galaxies (5000 baryonic particles or more). We sum up their basic properties and plot a Tully-Fisher relation. We find that smooth accretion of intergalactic cold gas dominates mergers for the mass growth of galaxies at $z < 2$. Next we study the baryonic accretion rate which shows different behaviours depending on the galaxy mass. The bias is also computed at different radii and epochs. Then we present galactocentric angular maps for the accretion integrated between $z = 2$ and $z = 0$, which reveal that accretion is highly anisotropic. Average accretion rates plotted against galactocentric latitude show a variety of behaviours. In general, accretion in the galactic plane is favored, even more for baryonic matter than for dark matter. Our results form a basis for prescribing realistic accretion in simulations of isolated galaxies.

1. Introduction

The most successful galaxy formation and evolution scenario is the hierarchical theory, which has been developed through semi-analytical models, based on the Press & Schechter (1974) formalism and its extensions (Bond *et al.* 1991, Lacey & Cole 1994, Kauffmann *et al.* 1993, Somerville & Primack 1999). In this theory, small irregular and disk galaxies form first, then merge hierarchically to produce larger and larger galaxies, ending up in giant ellipticals. The mass is dominated by collisionless dark matter, whose halos continue to hierarchically merge and form groups and clusters. In this model, the present morphology of a galaxy is intimately linked to the history of its interaction with the extragalactic environment through mergers. However other types of interactions, such as smooth accretion (the only contribution in the monolithic collapse model) and stripping, are equally important.

This is true in particular to explain galaxy disks, where smooth accretion must prevail (e.g. Abadi *et al.* 2003). If the hierarchical clustering picture is simple and success-

ful for collisionless dark matter, the physics of baryons is much more complex, including star formation and feedback, and the morphology of present day galaxies are not dominated by mergers, although they can still accrete tidal debris from a previous event.

This connection between morphology and environmental history can be studied both by observations and numerical simulations. Recently studies have been carried out of the fraction of each morphological type as a function of redshift in observed galaxies (see, e.g. Lilly *et al.* 1998, Van den Bergh *et al.* 2001). However, many possible observational biases make the interpretation difficult. In a more targeted work, Zabludoff & Mulchaey (1998) find from observations a high proportion of disk galaxies in poor clusters and infer that the merger rate is lower in poor clusters where galaxies represent a smaller fraction of the total mass. It is consistent with the picture where dynamical friction is a critical factor for the determination of the merger rate. This is an example of the crucial role of the cosmological environment on the morphological type of galaxies.

Morphological features such as bars and polar rings are strongly dependent on the environment. Important

Send offprint requests to: B. Semelin, e-mail: benoit.semelin@obspm.fr

constraints can be derived for example from the issue of bar formation and destruction. Several authors (Van den Bergh *et al.* 2001, and refs. therein) observed a deficiency of barred galaxies at high redshift. In a recent work, however, Sheth *et al.* (2003) find that this deficiency could be a bias due to insufficient resolution, and Jogee *et al.* (2004) found evidence for a constant bar frequency with time. In this case it is necessary to find a process that allows bar reformation since bars are known to dissolve in a few Gyr (Hasan, 1991). Bournaud & Combes (2002) find from N-body simulations that a sufficient rate of gas accretion from the intergalactic medium allows bars to reform.

In these two examples the competition between smooth accretion of intergalactic gas onto galaxies and mergers of galaxies plays a key role. The first favors (barred) spiral galaxy formation, the second favors the evolution toward elliptical galaxies. Moreover both are necessary to reproduce some morphological features. Kobayashi (2004) shows from numerical simulation that both mergers and accretion are necessary to reproduce observed radial metallicity gradients in galaxies.

Then galaxy mass assembly raises the following question: on average, how much of a galaxy's mass is gained by smooth accretion, and how much by mergers? Murali *et al.* (2002) give the following answer from numerical simulations: at $z = 2$ accretion dominates mergers by a factor of 4, this value drops to 2 at $z = 0$. This is an interesting result since accretion tends to be overlooked in the face of the successes of the hierarchical theory which emphasizes merging. Our aim in this work is to describe in detail the properties of accretion of both baryonic and dark matter onto galaxies in a cosmological framework. Aubert *et al.* (2004) study the geometry of dark matter accretion on a very large set (up to 5.10^4) of moderately resolved ($5.10^9 M_{\odot}$) massive halos. Our approach is complementary; we look at the properties and geometry of accretion of both baryonic and dark matter in a small set of well resolved individual galaxies ($6.410^6 M_{\odot}$ of baryonic mass resolution). To achieve this goal we have developed a new numerical technique.

To study detailed properties such as the anisotropy of accretion on a galaxy in a cosmological framework, we need a simulation which spans a scale range from 1 kpc to 10-100 Mpc. This has become possible in recent years with N-body treecodes or AMR codes on parallel supercomputers. In the case of N-body simulations the usual method is the following: a first cosmological simulation is performed where poorly resolved galaxies are identified, then a second simulation zooms in on the interesting regions (Navarro & White 1994). In this method as well as in AMR codes, the key idea is adaptative refinement of the simulation to spend CPU time where it is needed: in interesting regions. We present in this work a new numerical method which fits in the same family of adaptative refinement methods. Using a treecode, we perform, for a given model, a series of N-body simulations (4 in practice) zooming recursively onto the studied object. The simulation box size decreases at each step while the resolution in-

creases. Matter inflow and outflow and the tidal field from matter surrounding the current box are read in from data recorded at the previous level. Using this method with 4 zoom levels, we can reach the necessary dynamical range on a single processor workstation. Our *multi-zoom* method is implemented for parallel computers using OpenMP.

In section 2 we summarize briefly the main aspects of our tree-SPH implementation and of our physical model for the baryonic matter, and we describe in details our *multi-zoom* method. In section 3 we describe a validation test: the collapse of a pancake. In section 4 the method is applied to study accretion on highly resolved galaxies. Section 5 is devoted to discussion and conclusions.

2. Numerical methods

Our code is designed to study galaxy formation within a cosmological framework with a detailed modeling of the baryonic matter physics. A usual Tree-SPH implementation is boosted by a new multi-zoom method allowing a dynamical range from 1 kpc to 10 Mpc and more, at relatively low CPU-cost. We model baryonic matter as a multiphase medium; we take into account two gas phases (cold and warm) and a stellar component, and follow energy and matter exchanges between these phases. Dark matter is also included with purely gravitational dynamics.

2.1. Tree-SPH implementation - brief summary

The core dynamical code is a tree-SPH similar to the Hernquist & Katz (1989) implementation. A detailed description of the code and a validation test (collapse of an initially static isothermal sphere of gas Evrard 1988, Springel *et al.* 2001) can be found in Semelin & Combes (2002). We use an opening criterion $\theta = 0.8$ and quadrupole expansion for the computation of the gravitational forces with the tree algorithm. We keep a constant Plummer softening and a constant time step at a given zoom level. But we decrease both the softening length and the time step as we zoom in (see section 4.1). Periodical boundary conditions are available using Ewald method (Ewald 1921).

In the SPH forces computation we use a spherically symmetric spline kernel (Monaghan & Lattanzio 1985), arithmetic average for the smoothing length $h_{i,j}$, and the simple viscosity scheme described by Monaghan (1992) with $\alpha = 1.$ and $\beta = 2.$ We use 25 SPH neighbors.

2.2. Multi-zoom technique

2.2.1. Algorithm

It is necessary to study galaxy formation within large scale cosmological simulations to take into account self-consistently such major processes as gas smooth accretion onto galaxies and mergers with other galaxies. The difficulty is to cover a dynamical range from less than 1 kpc, necessary for disk dynamics, to a few tens of Mpc

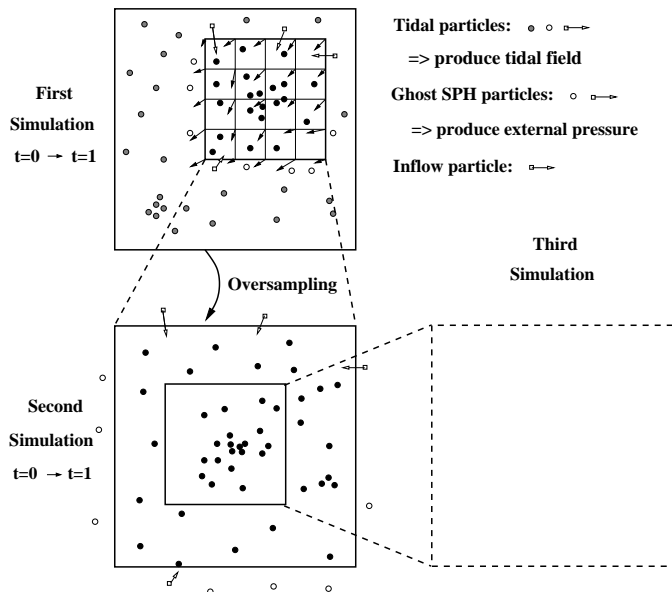


Fig. 1. The multi-zoom method. The simulations are run one after the other with increasing mass resolution in smaller and smaller regions, using data recorded in the previous simulation to take into account the action of matter surrounding the simulation box.

where the galaxy distribution tends to homogeneity. This requires high mass resolution which comes at a high CPU cost. Specific numerical techniques have been developed to reduce this cost. Navarro & White (1994) give a first zooming procedure which has been widely reused. A first cosmological simulation is run at moderate mass resolution. A galactic halo is identified at the present time and particles belonging to the halo are traced back to their initial positions, defining a zooming region. Initial conditions are then oversampled in this region, and under-sampled outside of the region to retain tidal interactions from surrounding matter at low CPU cost. A second simulation can then be made at higher mass resolution. One limitation of this method is that the mass resolution difference between the two simulations cannot be too large. Indeed if it was, and if we used an oversampled region tightly defined around the region of interest, the interaction with very massive particles outside the zoom region would create artificial perturbations. One way to alleviate the problem is to use gradually increasing mass resolution toward the center of the galaxy. But in practice, this requires several zooming simulations: indeed the central, very high resolution region boundaries cannot be correctly defined from the coarse cosmological simulation. Following this idea we have developed a new numerical method.

We run a first simulation in a cosmological cubic volume and *record* the tidal field in a sub-region at each time step. We sample the tidal field on a grid, at a resolution consistent with the mass resolution of the simulation. The tidal field is computed at each point of the grid by considering this point as a virtual particle and using the same tree algorithm as for the usual gravitational force computation. Of course, only particles outside the sub-region

are included when we build the tree and thus contribute to the tidal field. We also record all the properties of the matter inflow (position, velocity, internal energy, etc...), and the positions of SPH *ghost-particles* just outside the sub-region boundaries, which interact with particles inside the sub-region. We have used cubic subregions, but any shape can be used.

Then, we run a new simulation limited to the sub-region which we have oversampled. The particles outside the sub-region are ignored: the dynamics inside the sub-region is computed taking into account the recorded data (tidal field, external pressure and viscosity from SPH ghost-particles, and matter inflow). The action of the tidal field for a given particle is computed by cloud-in-cell interpolation of the recorded grid-values. This gives very accurate values in the center of the zooming region, but can produce small errors near the boundaries, when small and massive clumps lurk just outside the region. SPH ghost-particles are first split to match the mass resolution of the sub-region. The newly split particles are distributed in a volume consistent with local density and density gradient. Local internal energy gradient is also taken into account to assign internal energies to the new particles. This procedure allows for smoother boundary conditions. Then, the split ghost particles are simply included in the neighbour search for the SPH particles in the subregion, and contribute, if relevant, to the pressure and viscosity. Their own motion however is fixed from the previous zoom level. Finally, new particles are introduced according to the recorded matter inflow. We have chosen to keep a single mass for any particle type, so each inflowing particle has to be split according to the mass resolution ratio between two zoom levels; 8 in our case. The 8 new particles are distributed around the recorded position in a volume consistent with the local density, and a velocity dispersion is added to the recorded velocity to produce a more a less virialized 8-particle clump.

The gravitational smoothing length is reduced by the same factor as the scale resolution between the initial box and the sub-region, a factor of 2 in our case. The adaptation of the time-step is a more complex issue; it depends on the dynamical properties of the simulated systems. In the case of large scale structures or interstellar clouds (above 1 Mpc or below 100 pc), there is a self-similar law for the free fall time: $t_{ff} \sim \sqrt{L}$ where L is the scale. In this case the time step should be proportionnal to the square root of the space resolution. However, we study galaxy formation and our scale resolution lies in between those domains so this relation does not apply. Lacking a simple model for the dependence on scale of the free fall time in this scale range, we choose a conservative value for the time step in the *smallest* sub-region, and we increase it linearly with the scale resolution in larger region(s).

Both tidal field and matter inflow are recorded at each time step of the initial box. Consequently they are updated only every 2 time steps (for a ratio of 2 in the time steps) in the sub-region simulation. At this stage, we do not make any time interpolation to update these data each

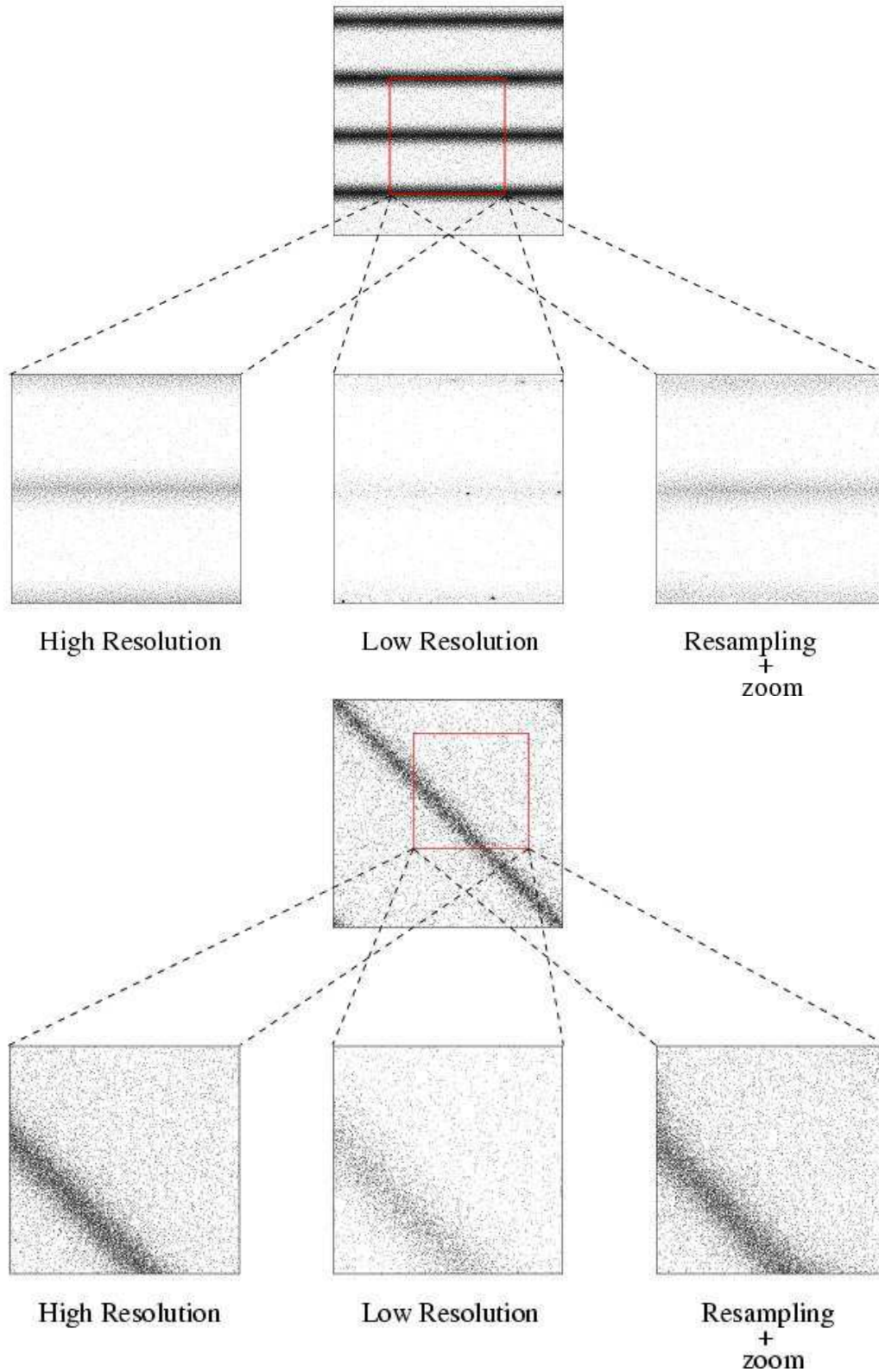


Fig. 2. Pancake formation. Particles are plotted at the instant when the shock steepening is maximal (see Fig. 3). Cases of pancakes either perpendicular to the boundary (upper panel) or tilted (lower panel) are presented. In each case, the top box shows the full simulation box in the high resolution simulation. The three bottom boxes show the zoom-in subregion in the high and low resolution simulations, and in the zoom simulation.

time step. This would be a possible improvement in the code for the future.

We apply this procedure *recursively*. In practice we have used up to 4 zoom levels reducing the box size by a factor of 2 at each level, and oversampling by a factor of 8. Using 32^3 simulations we obtain a mass resolution equivalent to a 256^3 simulation, although only over a small (but interesting) fraction of the initial volume. However, since we usually zoom in where galaxies are created, the inflow of matter can bring the number of particles up to 100^3 at the last zoom level in a large cluster. Fig. 1 presents a schematic view of the method.

2.2.2. Performance and reliability

The code is a usual Tree-SPH implementation, it shows standard performances for such codes. The overhead connected to computing, recording and re-using the tidal fields and matter inflow is limited: no more than 25 % of the total CPU time. The code is parallelized using OpenMP, it shows almost perfect scaling up to 16 processors for weakly clustered initial conditions. For highly clustered conditions the speed-up factor drops to 5 for 8 processors. This will be improved upon in future simulations. The cosmological simulations in this work were performed on 8 processors using an IBM SP4 at IDRIS (CNRS computing center).

The first obvious reliability question is the use of a recorded tidal field. The oversampling produces (small) modifications of the matter distribution in the zooming box and we do not take into account the feedback of these modifications on the dynamics of the matter outside the zooming box. This is the main difference to Navarro & White's method. We expect this feedback to be especially small in cosmological simulations in the non-linear regime, as long as we zoom in on density peaks. Indeed, in this regime, the internal dynamics of different clusters are largely decoupled. However, to check the robustness of the method, we have run a simulation in a difficult test-case where structures extend beyond the zooming box, see section 3. We have also checked that in a similar *static* situation, the reconstruction of tidal forces by interpolation produces errors smaller than the average error on the gravitational force due to the multipole expansion in the tree evaluation. Consequently we are confident in the reliability of our multi-zoom technique.

However, it does have some limitations. Obviously, some information is missing when a density structure crosses a boundary from low resolution to high resolution regions: fine details of the structure, absent in the low resolution region, cannot be recreated. Only subsequent evolution will produce such details. This limitation also exists in Adaptive Mesh Refinement codes. Navarro & White's method is not affected by this limitation in the same way since the boundary moves in with the matter flow and there is no particle splitting. One consequence is that mergers will be best described if the two components

have both formed in the last-level zooming box. In practice it puts a limit on the number of useful zoom-levels: about 4 in our case, for a 20 Mpc initial box. A larger initial box will allow more levels.

2.3. Physical model

The multi-phase physical model was detailed in Semelin & Combes (2002). The basic idea is that the interstellar medium (ISM) and inter-galactic medium (IGM) present a multiphase structure at scales below the resolution of numerical simulations. Cold dense gas clouds move almost as ballistic particles in a warm diffuse gas medium which behaves as a fluid. We attempt to model this sub-grid physics with macroscopic recipes, as is treated star formation in simulations on galactic and larger scales (e.g. Katz 1992, Mihos & Hernquist 1994). Multiphase models have recently received some attention (see, e. g. Springel & Hernquist 2003, Robertson *et al* 2004, Marri & White 2003).

Let us review our model briefly. We consider four phases: dark matter and stars, subject to gravity only, warm gas, subject to gravity and hydrodynamics (SPH), and cold gas, subject to gravity and collisional dissipation (for justifications see Semelin & Combes, 2002). Warm gas can cool radiatively and turn into cold gas at the 10000 K limit. Cold gas thermal evolution is not considered. Cold gas forms stars at a rate fixed by a Schmidt law (index 1.5). Thermal and kinetic feedback from supernovae on surrounding cold and warm gas particles is included: the affected cold gas particles are transformed back into warm gas particles. The surrounding medium is heated and receives a radial impulsion from the supernova. A non-instantaneous stellar mass-loss scheme is used (Jungwiert *et al.*, 2001) to return metal-enriched matter from the stars to the warm gas.

3. Pancake-formation test

To test the efficiency of our zooming method, we perform two demanding tests involving a strong gravitational tidal field and hydrodynamical shocks: the collapse of a pancake structure (Zeldovich 1970). In these tests initial perturbations develop and collapse in a sheet-like structure.

We start with a homogeneous distribution of motionless particles in a 3D cube of size 1 (total mass is 1. and $G=1$). To avoid grid effects we use the following procedure. Each particle is positioned at random and the system is relaxed using a repulsive gravitational force. This results in a glass-like homogeneous distribution. Two sets of initial fluctuations are then produced. The first is obtained by applying the following displacement: $\delta x = -0.025 \sin(6\pi x)$. This produces 3 pancakes perpendicular to the box boundary. The second is obtained by applying a displacement $-0.025 \sin(4\pi(x + y))$ to both x and y axis. This produces a diagonal pancake. Periodic boundary conditions are used. Cosmological expansion is ignored for this test. The initial internal energy is 0.01 in

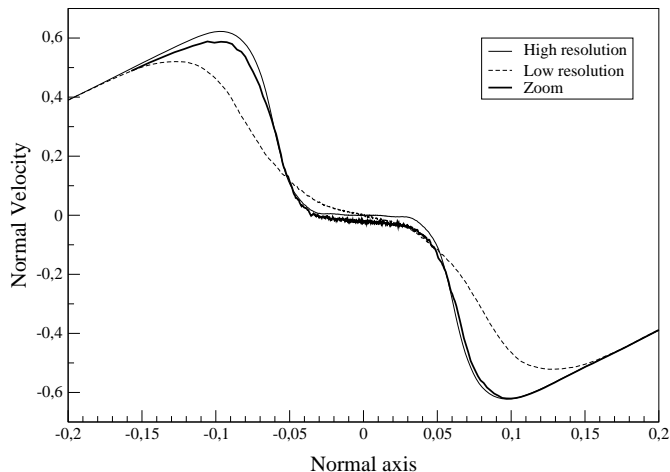


Fig. 3. Velocity profile for the tilted pancake collapse test, at $t=0.76$, close to the instant of maximal steepness of the two inward traveling shocks. The shock is steeper in the high resolution than in the low resolution simulation due to the SPH weak shock capturing abilities. The zoom simulation reproduces the high resolution simulation velocity profile with very good accuracy for the right hand shock where matter has crossed no boundary. The left hand shock in the zoom simulation occurs in gas which has crossed the boundary and is affected by the low resolution dynamics.

the first case and 0.03 in the second case (to counter a higher mass in the single pancake), and radiative cooling is turned off (adiabatic evolution). In the first case, high resolution is 50^3 and low resolution 25^3 gas-particles. In the second case, high resolution is 64^3 and low resolution 32^3 gas-particles. Then we zoom in on the central pancake in the low resolution simulation, in a cubic subregion of size 0.5. The zoom region is centered on the pancake in the first case, and off center in the second. In both cases, we resample the initial conditions to have the same mass resolution than in the high resolution simulation and use the recorded tidal field and inflow. The result of the simulations can then be compared in the central subregion.

Fig. 2 displays the particle distribution for the three simulations at $t=0.85$ in the first case and $t=0.76$ in the second case. In the perpendicular (first) case, the pancake structure in the zoom simulation shows no noticeable defect. In the tilted case, the structure is globally reproduced, but two small defects appear: two overdense tails extend out of the pancake along the boundaries on the side facing the center of the box. Additional simulations have shown that these tails are due to pressure forces: they disappear for dust or very low internal energy. Indeed matter in these regions feel the pressure of the pancake outside the sub-region, which, computed at a lower resolution, has a shallower profile. This is an unavoidable effect of the resolution transition. This defect is greatly enhanced by the fact that the structure remains motionless on the boundary: the ef-

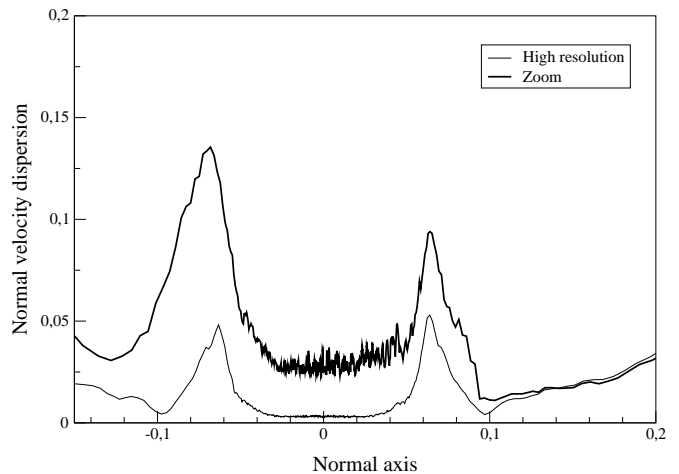


Fig. 4. Velocity dispersion profiles in the tilted pancake collapse test. The zoom simulation shows a higher velocity dispersion than the full high resolution simulation in the pancake region.

fect builds up over time on the same particles, preventing them from flowing out. This situation is very unlikely in cosmological simulation where we zoom on collapsing regions where structures flow through the boundary. In the test, no defect appears in the structure of the pancake on the side where inflowing gas accretes.

In these tests, the most sensitive diagnosis is the velocity profile, which exhibits hydrodynamical shocks. Fig. 3 shows the velocity profile at time $t=0.76$ in the case of the tilted pancake, the most difficult one. This instant is chosen to be close to the instant of maximal steepness in the shock fronts. Let us first notice that the two shock fronts are shallower in the low resolution simulation than in the high resolution simulation: its limited shock capturing ability is a well-known drawback of the SPH method. The zoom simulation gives a velocity profile which is very close to the high resolution simulation for the right hand shock where accreting gas comes from inside the sub-region. The left hand shock is a little bit less well reproduced. Indeed it accretes gas from outside the sub-region, whose earlier dynamics was computed at lower resolution. The resulting zoom shock is a little bit shallower than the full high resolution shock. From this diagnosis, we would say that the zooming method reproduces velocity profiles quite well even in region of inflowing gas. What about velocity dispersion?

In Fig. 4 we can see the velocity dispersion profiles for the high resolution simulation and zoom simulation. The dispersion is higher in the zoom simulation than in the high resolution simulation by a factor of 2 to 3 in the shock regions, and 5 or more in the center of the pancake. In the center of the sub-region (i.e. coordinate ~ 0.14 on the axis normal to the pancake in Figs 3 and 4), far from the boundary and not directly within the hydrodynamical shocks, the two velocity dispersions are almost identical. We believe that both the resampling of inflowing parti-

cles and the noisy (unrelaxed) distribution of ghost SPH particles are responsible for the increase in the velocity dispersion. The density structure itself however is not visibly affected by the velocity dispersion difference, which is important for galaxy formation.

4. Galaxy formation: properties of the accretion

We present now an application of our multi-zoom method to galaxy formation, focusing on the accretion of intergalactic matter onto galaxies. Our goal is to describe the geometrical properties of baryonic and dark matter accretion for well resolved galaxies. We achieve the necessary scale range by using 4 zoom levels. To obtain the same range on a single level, we would need 256^3 particles, and a supercomputer to run the simulation. With the multi-zoom method each 4 zoom level series of simulations (one per investigated region) required about 200 to 300 hours of single processor CPU times. A single zoom level in a particular region holds from 32^3 to 100^3 particles depending on the matter inflow during the time of the simulation.

4.1. Cosmological model and initial conditions

We use a flat Λ -CDM cosmological model with $\Omega_\Lambda = 0.7$, $\Omega_0 = 0.3$. The Hubble's constant at present time is $H_0 = 70 \text{ km s}^{-1} \text{ Mpc}^{-1}$, and the baryon density $\Omega_{\text{bar}} = 0.05$.

The power spectrum of primordial density fluctuations is $P(k) \propto k^{-2}$, normalized to $\sigma_8 = 0.8$. The power spectrum is predicted in a Λ CDM model to vary with scale k , from $n=1$ at large scale, until $n=-3$ at very small scale. From linear theory, and starting from a scale-invariant spectrum, as predicted by standard theories of inflation, it is possible to compute $P(k)$, which is in the above hypothesis, very close to $P(k) \propto k^{-2.5}$ for $0.1 < k(\text{Mpc}^{-1}) < 10$ and close to $\propto k^{-1}$ for $0.01 < k(\text{Mpc}^{-1}) < 0.1$ (Klypin *et al.* 1993). We adopted a constant slope of $n=-2$, fitted to the range of scales that we simulate. This approximation is not crucial in the computations done here, since we are in the highly non-linear regime, where the evolution modifies significantly the initial slope; in particular, non-linear effects will increase power on small-scale, especially strongly for $n < -1$ (Peacock & Dodds 1996).

We apply the usual procedure to produce the initial conditions at the first zoom level. We put particles on a grid and we compute their displacement and velocity according to Zel'dovich approximation to produce the desired fluctuation power spectrum, at the initial redshift of the simulation, $z = 45$ in our case. A simple way to produce the initial conditions for the successive zoom levels would be to compute the initial displacement field in the whole box at the resolution of the last zoom level, and extract initial conditions for all zoom levels from this field. Although this would be possible in our application with 4 zoom levels (256^3 grids to manipulate), it would become prohibitive in term of CPU with a few more zoom levels, or with a larger number of particles in the first level. Consequently we compute initial conditions recur-

sively from first to last zoom level: at each level we read in displacements due to large scales stored at the previous zoom level, we add the displacement from the new small scales introduced at this zoom level, and finally we store the displacement for the next zoom level. Of course, we ensure that the added fluctuations at each zoom level follow the desired power spectrum. The advantage of this method is that the cost is linear in the number of zoom levels.

At the first zoom level we use 32^3 particles, half baryons, half dark matter, distributed in a $20h^{-1} \text{ Mpc}$ box. This gives a baryonic mass resolution of $\sim 3.3 \cdot 10^9 M_\odot$. Then, at each zoom level, we reduce the box size by a factor of 2 and increase the mass resolution by a factor of 8. The baryonic mass resolution at the fourth zoom level is $\sim 6.4 \cdot 10^6 M_\odot$. Since we focus the zooms on the local overdensities where the galaxies form, we end up at the 4th zoom level with simulations involving 10^5 to 10^6 particles, due to matter inflow. For zoom level 1 to 4, we use a gravitational softening of 20, 10, 5 and $2.5 h^{-1} \text{ Mpc}$ and a timestep of 10, 5, 2.5 and 1.25 Myr.

4.2. Gas cooling in a cosmological framework

One of the focus of our simulations is the separation between a warm and a cold gas phases with different dynamics. In Semelin & Combes (2002) we have studied in details the exchanges between the two phases within a galactic disk. This study is also relevant at cosmological scales, but new behaviours appear. First, at high redshift, adiabatic cooling due to cosmological expansion dominates the cooling of warm gas. This mechanism is so effective that, if not counterbalanced by first star formation, all the warm gas turns into cold gas early on. Since the mass resolution is not sufficient to produce early star formation leading to the reionization of the universe, the reionization is introduced artificially using a constant heating of cold gas particules (those below 10 K) between $z = 15$ to $z = 6$. Cold gas will then replenish the warm gas phase, and a sizeable fraction of warm gas survives the fast-expansion era.

To summarize, warm gas is turned into cold gas both where collapse occurs in high density regions (through radiative cooling) and in low density, dynamically quiet regions (through adiabatic expansion). Warm gas survives mostly in dynamically active (turbulent) regions around density peaks, where it is heated first by reionization, and later by hydrodynamical shocks. It forms a diffuse halo. The different morphologies of warm and cold gas phases can be seen on fig. 5. The warm gas phase is also replenished at smaller redshift by star formation feedback. However, without a proper treatment of radiative transfer including the propagation of ionisation fronts, this feedback energy is closely confined around star-forming galaxies and is not transported into the inter-galactic medium.

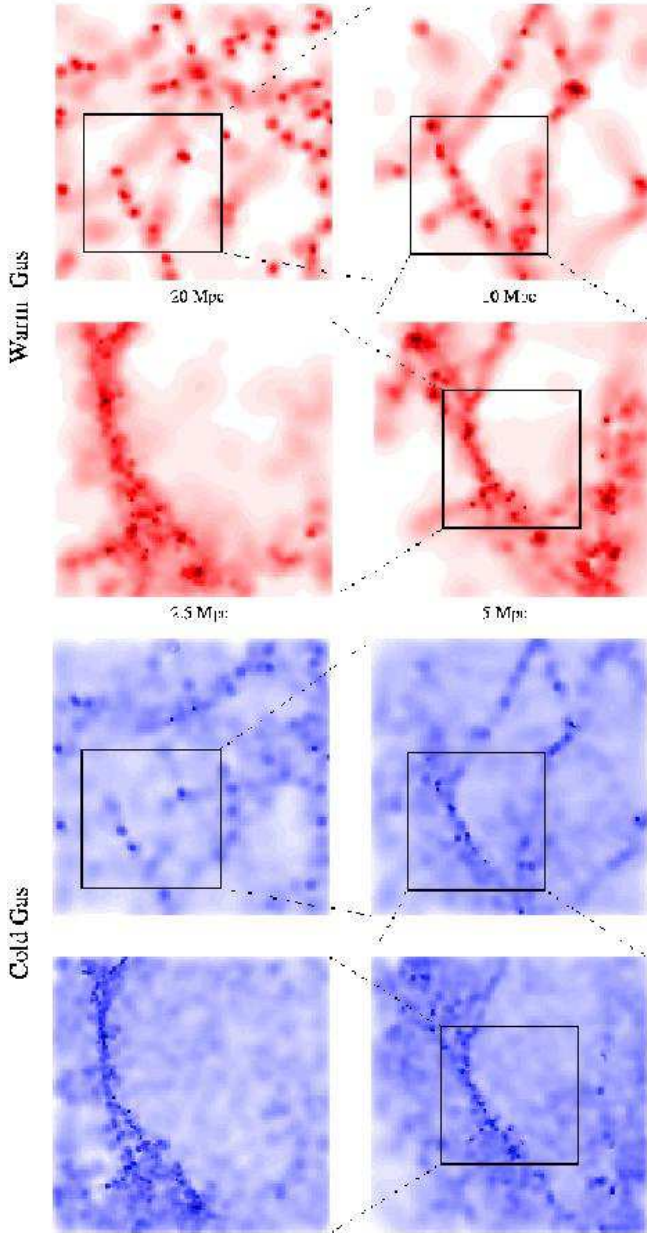


Fig. 5. Warm and cold gas phases density fields over 4 zoom levels (20, 10, 5 and 2.5 kpc box sizes) at $z \sim 1.57$. The focus is on the region where galaxies number 4 and 5 are found (see Table 1). The density fields are computed from the gas particle positions using an SPH-like adaptive smoothing. White cores represent high density regions and dark areas are voids. The different dynamics of warm and cold gas (SPH vs sticky particles) produce different density structures: rather diffuse for the warm gas, more clumpy for the cold gas.

4.3. Galaxy identification and basic properties

We have investigated 8 regions down to the fourth zoom level. Among them, 6 regions provide good galaxy candidates. The region where positioned *by hand*. Then we apply a clump finding algorithm to the 6 regions. We use a *friend of friend*-like algorithm (e.g. Huchra & Geller,

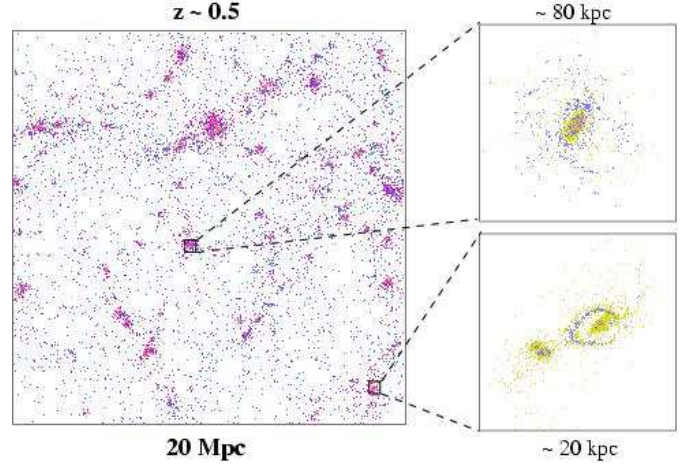


Fig. 6. Example of field galaxies selected for our study (number 1 on top and number 8 at bottom) at $z = 0.5$. Magenta particles are dark matter particles, blue particles are cold gas particles and yellow particles are stars (electronic version only). Dark matter is not plotted in the two zooms. Galaxy 1 (face-on) exhibits an extended cold gas disk, and a stellar disk growing from inside out. There is little bulge to speak of: the extent of gravitational softening prevents its formation. Galaxy 8 is undergoing a merger.

1982). We compute a SPH density for *all* (even non-gas) particles. Then we select local density maxima (particles with a higher density than their SPH neighbours), and starting with the highest maximum, we build the clump by accreting neighbouring particles with lower density (friend of friend part) which are above a given density threshold (the average density) and do not already belong to another clump. Then we remove from the local maxima list the clumps which are below a given number of particle threshold (500 particles here). We iterate the process 5 times, re-sorting the order in which we examine the clumps by decreasing mass. We applied this algorithm to the six regions at $z = 2$, and identified 10 galaxies with a mass within a factor 10 of the Milky Way mass. We rejected dwarf galaxies since we want $\sim 10^4$ baryonic particles per object. Another criterion for rejecting galaxies was crossing, or being too close to the boundaries of the zooming box. Indeed we wish to minimise the impact of accretion of matter which underwent a change in mass resolution.

The masses of the selected objects at $z = 0$ are given in Table 1. Two examples of this selection process are shown on fig. 6.

Let us make a few remarks about the disk structures formed in the simulation which can be seen in Fig. 6. First, cold gaseous disk do form, and have spiral arms. A stellar disk forms from inside out. Warm gas is only present through the local feedback of star formation. Fig. 7 shows the Tully-Fisher relation for 9 of the 10 galaxies (the last galaxy shows no definite rotation). The maximum rotation velocity is computed by a procedure similar to observations: an histogram of velocities along a line of sight is

Galaxy	Group	Baryonic mass in M_{\odot}	Gas fraction	τ_{ac} in Gyr	Mass growth by mergers
# 1	L	$1.0 \cdot 10^{12}$	19.1 %	-	< 5%
# 2	S	$6.2 \cdot 10^{10}$	2.2 %	1.7	21%
# 3	L	$1.9 \cdot 10^{12}$	24.4 %	-	25.5%
# 4	M	$4.0 \cdot 10^{11}$	12.6 %	4.7	55%
# 5	S	$3.7 \cdot 10^{10}$	3.6 %	1.3	9%
# 6	M	$1.9 \cdot 10^{11}$	16.5 %	21.4	40%
# 7	S	$9.0 \cdot 10^{10}$	10.0 %	4.4	7.5%
# 8	M	$3.4 \cdot 10^{11}$	7.3 %	8.9	12.5%
# 9	M	$3.1 \cdot 10^{11}$	16.0 %	-	25%
# 10	L	$1.1 \cdot 10^{12}$	11.5 %	-	63%

Table 1. Basic properties at $z = 0$ of identified galaxies. They are classified in 3 groups according to final mass, S for small, M for medium and L for large. The baryonic mass is computed within a $50 h^{-1}$ Mpc radius at present time. The gas fraction is the percentage of hot+cold gas to total baryonic matter within a $50 h^{-1}$ Mpc radius at present time. τ_{ac} is the decay time of smooth accretion rate for baryonic matter (see main text). The mass growth from mergers is the fraction of baryonic mass acquired between $z=2.$ and $z=0.$ by mergers with a mass ratio greater than $\frac{1}{20}$.

computed for gas particles, the inferred rotation velocity is half the width of the histogram at 20 % of the maximum value. This procedure is repeated for a large number of random lines of sight, and the maximum value of the velocity is retained. The law fitted from observations is plotted as a full line. The slope is taken from Giovanelli *et al.* (1997), 0.325 on our graph, and the zero point is the Milky Way with baryonic mass $2 \cdot 10^{11} M_{\odot}$ and maximum rotation velocity 220 km.s^{-1} . This plot should be interpreted with care since all but the 3 largest galaxies have disks with radii smaller than 3 times the gravitational softening. With this in mind we can check that, the Tully-Fisher relation of the numerical galaxies has a correct slope but a shifted zero point, which is similar to the detailed study by Navarro and Steinmetz (2000). The rotational velocity excess is connected to the angular momentum problem: disks are too small because of a large loss of angular momentum towards the dark matter halo. The problem may be alleviated and large disks may be obtained by modifying the equation of state for the gas, as suggested by Robertson *et al.* (2004).

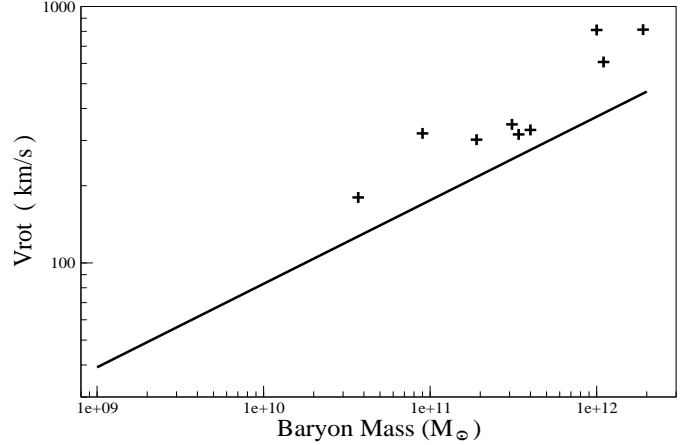


Fig. 7. Tully-Fisher relation for 9 of the 10 identified galaxies in the sample, at $z = 0$. The maximum rotation velocity in the gaseous disk is plotted against the baryonic mass of the galaxy. The full line represents a fit through observed galaxies (e.g. Giovanelli *et al.* 1997).

In any case, accretion at more than 50 kpc from the galactic center, which is the main focus of this paper, is hardly affected by the disk size.

4.4. Baryonic mass accretion rates

From $z = 45$ to $z = 0$, we produce 108 outputs for each investigated region. Using the outputs we can compute the mass accretion rates with a 125 Myr time resolution. For each output, the baryonic mass of the 10 galaxies is computed within a $50 h^{-1}$ Mpc radius. Only particles which are also present in the last output contribute, to avoid the contribution from bodies on hyperbolic orbits.

Let us first comment on the fraction of mass gained through mergers. Table 1 gives rough estimates (derived from sharp steps in mass growth histories) of the contribution of mergers between $z = 2.$ and $z = 0.$ Only mergers with mass ratio larger than $\sim \frac{1}{20}$ are identified in this estimate. Bournaud *et al.* (2004) find that mergers with a mass ratio smaller than $\sim \frac{1}{10}$ have very little effect on the morphology of the large galaxy because the small galaxy is ripped apart before hitting the large one. Consequently mergers with mass ratio of $\sim \frac{1}{20}$ and lower indeed qualify as smooth accretion. Although we find a wide scatter in the contribution of mergers to the mass growth, from a few percent to 63%, our results agree on average with values given by Murali *et al.* (2002). The bottom line is that, in general, smooth accretion dominates mergers as far as mass growth is concerned.

Fig. 8 shows the smooth accretion rate histories in solar masses per year. There is one graph for each group, Small, Medium and Large, and one curve for each galaxy. Mergers, which produce spikes in the accretion rate history, have been removed leaving only smooth accretion.

First, the average gas accretion rates computed for our sample of galaxies, typically in the range $1 - 100 M_{\odot} \text{ yr}^{-1}$ for galaxies with a final mass from $3 \cdot 10^{10} M_{\odot}$ to $2 \cdot 10^{12} M_{\odot}$

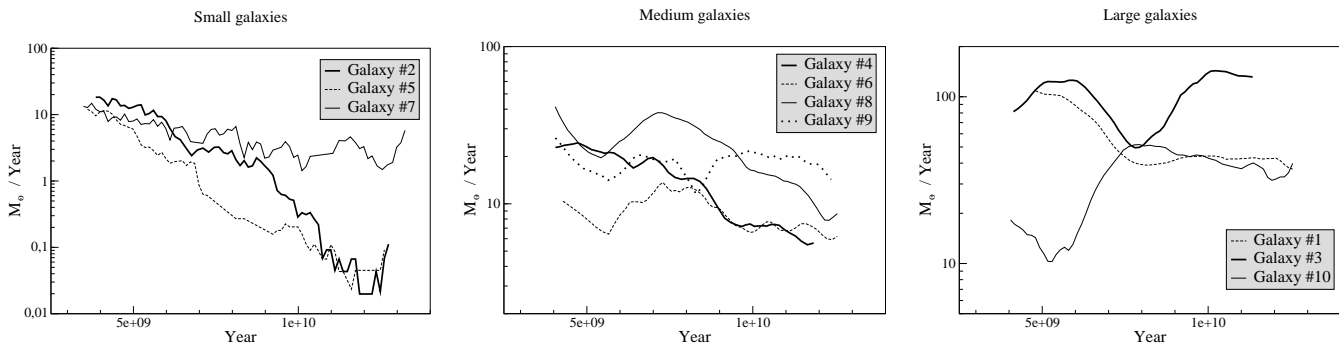


Fig. 8. Baryonic accretion rate in M_{\odot} per year for sample galaxies in group S, M and L. Mergers have been removed from the plots. The curves have been smoothed over 100 Myr periods.

are in the same range as observed for star formation rates. Moreover, visual inspection of the output snapshots shows that the smoothly accreted baryonic mass is almost exclusively cold gas. This suggests that accretion replenishes the gas phase in the disk, and may actually regulate the star formation rate. Finally let us mention that our computed accretion rates are sufficient to produce the reformation of bars according to Bournaud & Combes (2002).

The accretion rate of the galaxies in the S group show a decreasing behaviour of the type $\dot{M}_{\text{ac}} = \dot{M}_0 \exp(-\frac{t}{\tau_{\text{ac}}})$. The fitted values for the typical decay time τ_{ac} are given in Table 1. Galaxies in group M, except one, show the same behaviour with larger values for τ_{ac} . Galaxies in group L have a more or less constant accretion rate (no systematic decay). Exponential decay type laws for the accretion rate suggest a simple model: the accreted matter is taken from a finite surrounding reservoir in quasi-equilibrium, at a rate proportional to the gas remaining in the reservoir. In this picture: it is slow angular momentum loss which drives accretion onto the galaxy (which leads to the angular momentum problem, Navarro & Steinmetz 2000). The process could be self-regulated: the presence of more gas in the galaxy triggers non-axisymmetric instabilities, such as bars, which drives the gas inwards. D’Onghia & Burkert (2004) find a different picture based on dark matter simulations where matter falls on eccentric orbits with little angular momentum in the first place; too little in fact to account for observed galactic spins even without angular momentum loss during accretion. A possible answer is that the dissipative dynamics of accreting baryons concentrates angular momentum more efficiently: the baryonic matter ending up in the galaxy is drawn from a larger reservoir than non-baryonic matter, thus has a higher initial specific angular momentum.

If star formation activity is a good tracer of the accretion rate, as we believe, these accretion rate histories are at odds with observations: real large galaxies in the center of clusters have little star formation activity at the present time, while dwarf galaxies keep forming stars at a good rate, relative to their mass. We find the opposite. We suggest two phenomena to explain this discrepancy. It appears that, in the simulations, the accretion rate of

the smallest galaxies decays too fast: this may well be caused by the well-known overmerging phenomenon. The smallest galaxies are the closest to the mass resolution limit, where overmerging is predominant; thus, they accrete all the available mass early on, and, because of their low mass, are not able to capture any more mass later on. In other words, they build up to their maximal mass too fast, then the accretion stops. As for large galaxies, which keep accreting too much mass in our simulations, the problem may arise from an inadequate heating of gas at large-scale. In real clusters, we observe a massive virialized hot gas halo (holding as much or even more baryonic mass than the galaxies, e. g. David *et al.* 1995), sustained by pressure, and only in the center, gas is able to cool down and infall onto the central galaxy (Fabian 1994). The importance of the feedback from the central AGN to moderate the cooling flow has now been realised (e.g. Brighenti & Mathews, 2003), and this feedback is not included in our simulations. Moreover, in rich groups and clusters, the hot gas halo (ICM) is stripping the interstellar medium of galaxies, and prevents cold gas accretion, quenching star formation (Poggianti *et al.* 1999). If such a halo is indeed present in the simulations, it is not massive enough. Taking into account radiative transfer and ionization fronts could alleviate the problem. Moreover, our spatial resolution is not enough to deal properly with ram pressure, which would contribute to gas stripping in rich environments, where massive galaxies are found.

We have shown that the average accretion rates have the expected values, but that accretion rate histories versus mass are affected by the limitations of the simulation. This, however, should not change drastically the geometrical properties of accretion that we study in section 4.6.

4.5. Bias

Numerical simulations have shown that the standard Λ -CDM model leads to overconcentrated dark matter halos compared with observations (Burkert & Silk 1997, Moore *et al.* 1998). The angular momentum problem (baryonic matter losing momentum to dark matter, resulting in too small galactic disks) has also proven difficult to overcome

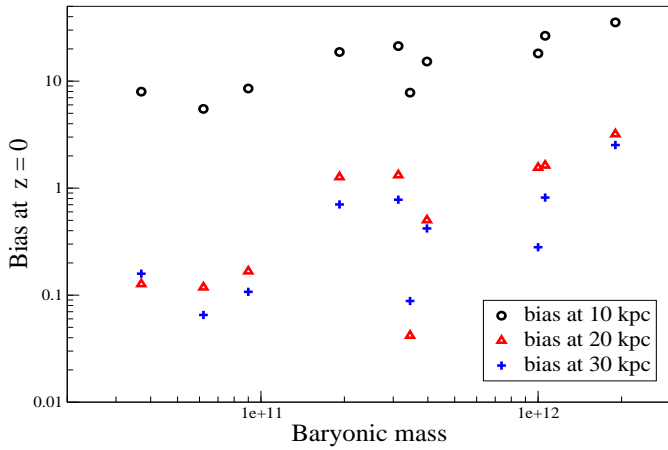


Fig. 9. The local bias, baryonic to dark matter mass ratio relative to cosmic abundance (ratio of 0.2), is plotted for each galaxy in our sample, with the masses computed within a 10, 20 or 30 kpc sphere, at $z = 0$.

(Navarro *et al.* 1995). The latter may arise from numerical issues only, but both are connected to matter accretion onto forming galaxies. A crucial diagnostic for the distribution of matter around galaxies is the local (those below 10 K) bias: that is, the local baryonic matter to dark matter mass ratio relative to the average cosmic ratio of $\Omega_b/\Omega_{CDM} = 0.2$. We have computed this diagnostic for the galaxies in our sample.

For each galaxy, we have computed the total mass of dark and baryonic matter within 10 kpc, 20 kpc and 30 kpc from the galactic center at $z = 0$. Then we have derived the corresponding local biases, which are plotted in fig. 9 against the baryonic mass of the galaxy as computed in Table 1. The first obvious effect is that bias decreases as radius increases: this is to be expected since baryonic matter is highly concentrated within dark matter halos. Next we can check that at a given radius, the bias increases with the galaxy mass. This is in line with observations which show that dwarf galaxies are dominated by dark matter (small biases) while intermediate and giant galaxies are not. The biases at 10 kpc which are less noisy than biases at 20 and 30 kpc (due to accreting gas clumps without dark matter haloes) even suggest a power law relation between the bias and the galactic mass. The quantitative value of the exponent may depend on the particular model and strength of gas dissipation. It requires a more thorough study.

In Fig. 10 we plot the evolution with time of the bias at 10 kpc for all the galaxy. Since we are interested in a common behaviour we did not identify individual galaxies on the plot, but as Fig. 9 shows, higher biases are associated with larger baryonic mass. The salient feature of Fig. 10 is that, after a strong initial rise, the bias slowly decreases with time. Baryonic matter accretes very fast during the initial formation era of the galaxy mass assembly, then drops and even stops in some cases at later times, while the dark matter halo keeps concentrating. The bias decay rate seems independent of the galactic mass at late times

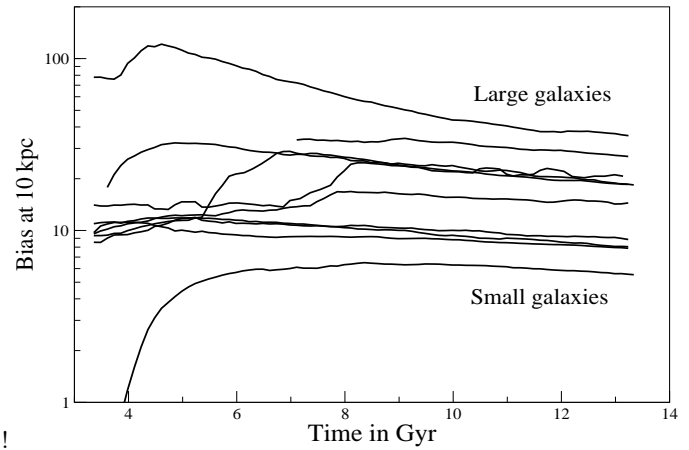


Fig. 10. The evolution of the bias at 10 kpc (see def in Fig. 9) of all the galaxies in our sample is plotted against time. Individual galaxies are not identified since we are looking for a common global behaviour. Large galaxies are at the top, small galaxies are at the bottom.

(between 10 and 13.7 Gyr). We computed the decay times; they change by a factor of more than 3 in the range of a few tens of Gyr.

4.6. Accretion maps

The geometry of accretion is an important issue. Is the accretion isotropic? Is it confined to the galactic plane or does it come from one or several intergalactic filaments in specific directions? To answer these questions we have plotted angular accretion maps. The galaxies are identified at $z = 2$. In subsequent outputs, those particles with a distance to the galactic center between $50 h^{-1}$ kpc and $100 h^{-1}$ kpc that have not been tagged as accreting particles in a previous output and that are within $50 h^{-1}$ kpc of the galactic center in the last considered output (at $z = 0$) are included in the accretion map: we record their angular position on a sphere centered on the galaxy. For each scanned output we reorientate the pole axis of our angular coordinates system with a single rotation from the previous orientation, to keep it parallel to the spin of the baryonic matter in the galaxy. The spin direction can change by 90 degrees over the life time of the galaxy.

Fig. 11 shows angular accretion maps for baryonic matter and dark matter for galaxies 2, 3, 8 and 9. We have computed the maps for all galaxies. Removing maps with poor definition or major mergers, we selected these four as typical cases showing the variety of accretion geometry. They reveal that accretion is neither isotropic nor always closely confined in the galactic plane. The accretion is very anisotropic and clumpy for baryonic matter, and somewhat smoother if not isotropic for dark matter. This reflects the global clustering properties of baryonic and dark matter.

These maps, integrated over ~ 10 Gyr, contain a few 10^4 particles. It would be interesting to have *instantaneous* accretion maps, integrated over much shorter periods (of

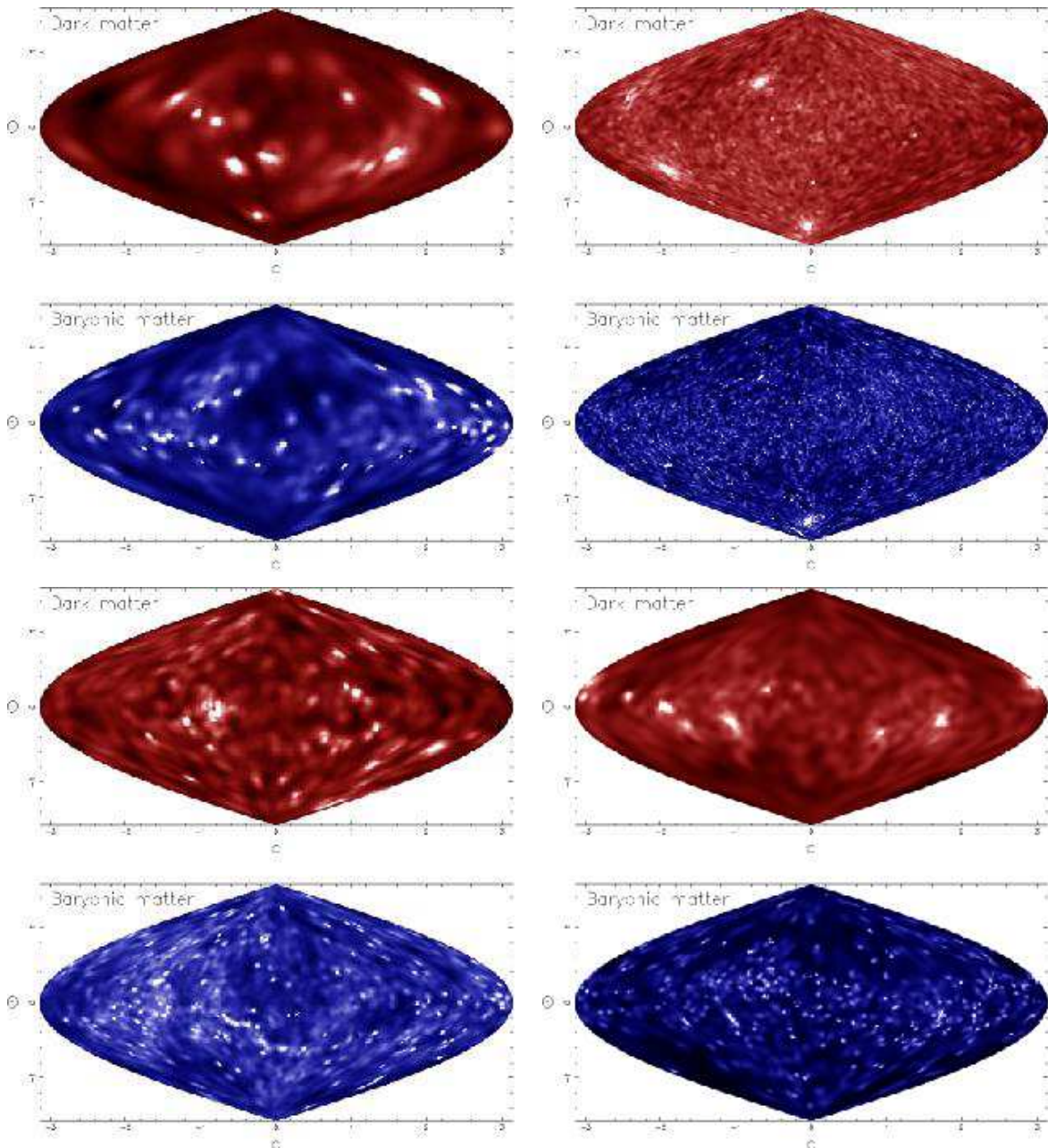


Fig. 11. Galactocentric accretion rate maps for galaxies 2,3,8 and 9 (left to right and top to bottom). Light is for high accretion, dark for low accretion. The maps are integrated between $z = 2$ and $z = 0$, with a polar axis reoriented to follow the angular momentum of the baryonic matter within 50 kpc of the galactic center. Accretion is detected in a 50 kpc to 100 kpc shell centered on the galaxy.

the order of a galactic rotation). However, at the current mass resolution of the simulations, these maps would be very poorly sampled. Studying the evolution of the accretion maps with time is very important, but will have to wait for higher resolution simulations.

To answer the simple question of whether accretion occurs mainly in the galactic plane or not, we have integrated the angular map along the longitude to plot the accretion rate as a function of galactic latitude. Minor mergers were removed before integration by applying a cut off at 2.5 times the average value of the angular maps. Thus the

accretion rates as function of latitude shown in Fig. 12 pertain to smooth accretion, not to merging events. The first observation is that galaxies 2, 3 and 9 baryonic matter accretion rates are stronger in the galactic plane than at high latitude by a factor of up to ~ 3 . This is not the case for galaxy 8, for which the galactic plane is not favored. The dark matter accretion rate seems to be flatter (less latitude dependent) than the baryonic matter accretion rate: this is obvious for galaxy 2, and also true for galaxy 1 if we neglect the two peaks linked to not-fully-removed mergers. Accretion rates for both types of matter

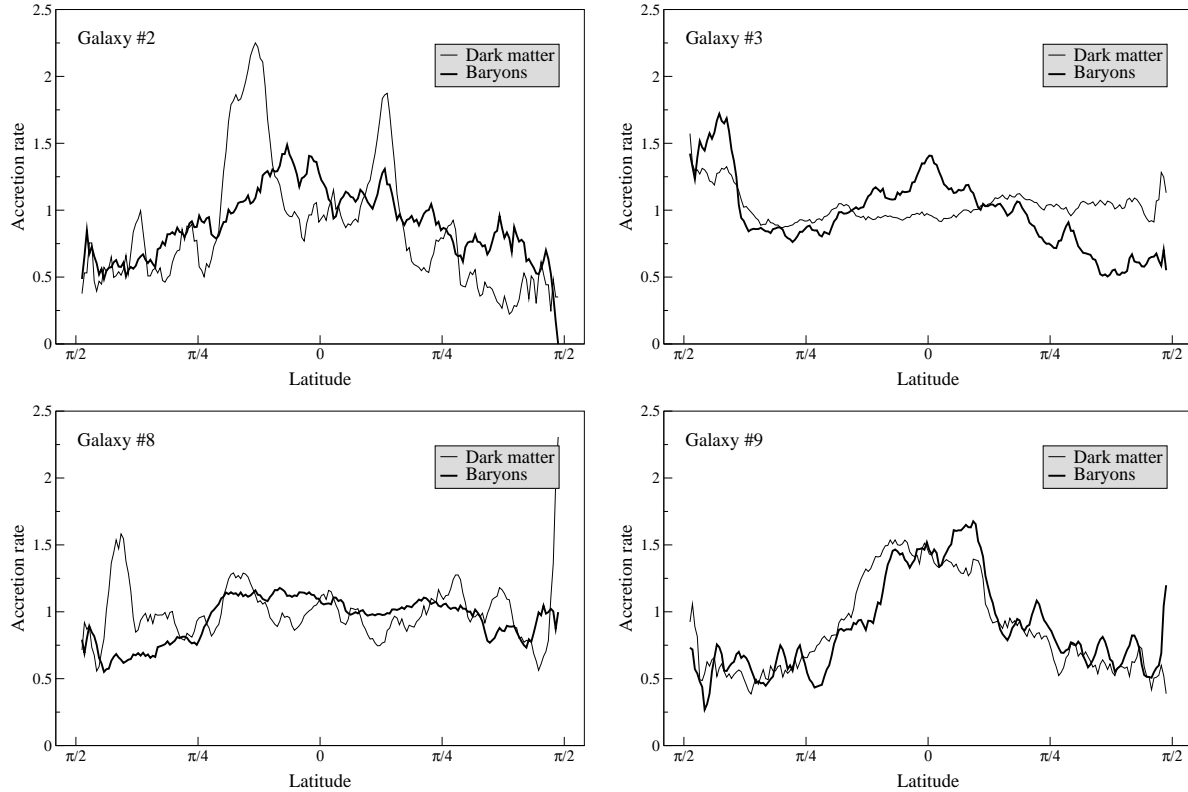


Fig. 12. Accretion rates as a function of galactic latitude for galaxies 2,3,8 and 9 (left to right and top to bottom). These maps are derived from Figure 11. Mergers have been removed to a large extent by cutting off maps in Fig 11 at 2.5 the average value of the map, then integrating along the longitude.

are rather flat for galaxy 8, and peaked at low latitude for galaxy 9.

Thus, accretion often seems to be stronger in the galactic plane for baryonic matter. While this also happens for dark matter, the anisotropy seems weaker. We have studied a few examples at high resolution; a statistical study at the same resolution is highly desirable. Then, connecting the degree of anisotropy to the environment would be possible.

5. Conclusion

Our goal in this work was to describe the detailed properties of accretion of baryonic and dark matter onto well-resolved galaxies in a cosmological framework. The competition between mergers and smooth accretion during the mass growth of galaxies depends on the local cosmological environment and determines the morphological evolution of the galaxy. Murali *et al* (2002) find that the mass gained by accretion dominates the mass gained through mergers by a factor of 2 to 4, on average. This factor is much larger for field galaxies. Consequently, characterizing accretion precisely is necessary. However studying accretion in a cosmological context requires us to span a scale range from 1 kpc to several tens of Mpc. To achieve this scale range, we have developed a new numerical approach; the *multizoom method*.

The key idea derives from traditional multiresolution techniques like AMR or the treecode + single zoom technique. We compute a series of successive simulations in smaller and smaller nested boxes at higher and higher resolution. At each level, we record the matter inflow for the next simulation box and tidal field on a grid for this box. We use the data recorded at the previous level to compute the contribution to the dynamics of the matter located outside the current simulation box. We do not take into account the feedback that the new structures created by the increase in mass resolution can have on external structures and their tidal action. To check that this feedback is negligible we ran a test simulation: the collapse of a self-gravitating pancake. We ran one high resolution simulation (64^3 particles), one low resolution simulation (32^3 particles) and one zoom simulation with inflow and tidal field recorded from the low resolution simulation. The zoom and high resolution simulations have the same mass resolution. We find that they give very similar results, away from the zoom simulation box boundaries. We present velocity profiles and velocity dispersion profiles of the hydrodynamical shocks which form during the collapse. The match between the high resolution and the zoom simulation is satisfactory.

The main advantage of the multizoom technique is the CPU cost: the high resolution dynamics are only com-

puted in a small fraction of the initial simulation box where the galaxy is located. We were able to run simulations with an equivalent resolution of 256^3 particles in 200 to 300 single CPU hours for each investigated region. Disk space is required to store the tidal field data, but it is not prohibitive. The method is implemented for parallel computers using OpenMP.

We have applied the multizoom method with 4 zoom levels (20, 10, 5 and 2.5 h^{-1} Mpc box size) and a multiphase Tree-SPH code to study the properties of accretion during galaxy formation in the cosmological environment. Using a friend-of-friend algorithm we have identified 10 galaxies with at least 5000 baryonic matter particles at $z = 0$. These galaxies range in mass from $3.710^{10} M_{\odot}$ to $1.910^{12} M_{\odot}$ and from 2.2% to 24.4% in gas fraction of the baryonic mass. We plotted a Tully-Fisher relation and found a correct slope with a shifted zero-point (similar to Navarro and Steinmetz 2000). We assume that this issue does not affect the properties of accretion at radii larger than 50 kpc, which is the focus of this work.

We estimate the contribution of mergers with a mass ratio larger than $\frac{1}{20}$ to the growth of the galactic mass for $z < 2$. We find that it is dominated by smooth accretion. Then we compute the evolution of the baryonic mass accretion rate with a 125 Myr time resolution, excluding merger events. We find accretion rates between 1 and $100 M_{\odot}/\text{yr}$ almost exclusively in the form of cold gas. These rates are in the same range as global star formation rates, suggesting that the accretion regulates the star formation rate by replenishing the gaseous phase in the galactic disks. Low mass galaxies show accretion rates with an exponential decay law with a typical time-scale of a few Gyr. Larger galaxies have sustained accretion rates throughout their lifetime. It is possible that numerical overmerging depletes the accretion reservoir of small galaxies early on, leading to fast decaying accretion. For large galaxies, inadequate modeling of feedback from AGN or ram-pressure stripping from the intracluster medium may lead to overestimated accretion rates at late times.

Then we plotted angular accretion maps for 4 typical galaxies. These maps are integrated between $z = 2$ and $z = 0$, which gives a few 10^4 particles per maps. They reveal anisotropic accretion, especially for the baryonic matter which accretes in the form of small clumps. To check systematic anisotropy we integrate along galactocentric longitude, obtaining accretion rates as a function of galactic latitude. We find a majority of cases with an accretion excess at low latitude, in the galactic plane. This is consistent with results from Aubert *et al.* (2004). The additional information is that the excess is larger for baryonic matter than for dark matter.

We have provided a few guide-lines to prescribe accretion around an isolated galaxy. Larger statistic samples and higher resolution are needed to confirm and extend these results.

Acknowledgements. We are grateful to Frédéric Bournaud and Romain Teyssier for interesting discussions. The numerical

simulations in this work have been realized on the IBM-SP4 of the CNRS computing center, at IDRIS (Orsay, France).

References

- Abadi, M. G., Navarro, J. F., Steinmetz, M., Eke, V. R.: 2003, ApJ 597, 21
- Aubert D., Pichon C., and Colombi S. 2004, MNRAS, 352, 376
- Bond J.R., Cole S., Efstathiou G., Kaiser N.: 1991, ApJ 379, 440
- Bournaud F., & Combes F. 2002, A&A, 392, 83
- Bournaud F., Combes F., and Jog C. 2004, submitted to A&A
- Brighenti F., & Mathews W. 2003, ApJ 587, 580
- Burkert A., & Silk J. 1997, ApJL, 488, L55
- David L. P., Jones C., and Forman W. 1995, ApJ, 445, 578
- D’Onghia E., Burkert A. 2004, ApJ, 612, 13
- Evrard A. E. 1998, MNRAS, 235, 911
- Ewald P. P. 1921, Ann. Phys., 64, 253
- Fabian A.C. 1994, ARA&A 32, 277
- Giovanelli R., Haynes M. P., Herter T., et al 1997, AJ, 113, 53
- Hasan H., & Norman C. 1990, ApJ, 361, 69
- Hernquist L., & Katz N. 1989, ApJS, 70, 419
- Huchra J., & Geller M. 1982, ApJ 257, 423
- Jogee S., Barazza F., Rix H-W. et al: 2004, ApJ 615, L105
- Jungwiert B., Combes F., and Palous J. 2001, A&A, 376, 85
- Katz, N. 1992, ApJ, 391, 502
- Kauffmann G., White S.D.M., Guiderdoni B.: 1993, MNRAS 264, 201
- Klypin A, Holtzman J, Primack J, Regös E: 1993, ApJ 416, 1
- Kobayashi C. 2004, MNRAS, 347, 740
- Lacey C., Cole S.: 1993, MNRAS 262, 627
- Lacey C., Cole S.: 1994, MNRAS 271, 676
- Lilly S., Schade D., Ellis R., et al: 1998, ApJ 500, 75
- Marri S., & White S. D. M. 2003, MNRAS, 345, 561
- Mihos, J. C., & Hernquist, L. 1994, ApJ, 437, 611
- Monaghan J. J., & Lattanzio J. C. 1985, A&A, 149, 135
- Monaghan J. J. 1992. Ann. Rev. A&A, 30, 543
- Moore B., Governato F., Quinn T., Stadel J., and Lake G. 1998, ApJL, 499, L5
- Murali C., Katz N., Hernquist L., Weinberg D. H. and Davé R. 2002, ApJ, 571, 1
- Navarro J. F., & White S. D. M. 1994, MNRAS, 267, 401
- Navarro J. F., Frenk, C. S., and White, S. D. M. 1995, MNRAS, 275, 56
- Navarro J. F., & Steinmetz M. 2000, ApJ, 538, 477
- Peacock J.A., Dodds S.J. 1996, MNRAS 280, L19
- Poggianti B., Smail I., Dressler A. et al.: 1999, ApJ 518, 576
- Press W. H., & Schechter P. 1974, ApJ, 187, 425
- Robertson B., Yoshida N., Springel V., and Hernquist L. 2004, ApJ, 606, 32
- Semelin B., & Combes F. 2002, A&A, 388, 826
- Sheth K., Regan M. W., Scoville N. Z. and Strubbe L. E. 2003, ApJ, 592, L13
- Somerville R., Primack J.R.: 1999, MNRAS 310, 1087
- Springel V., Yoshida N., and White, S. D. M. 2001, NewA, 6, 72
- Springel V., & Hernquist L. 2003, MNRAS, 339, 289
- Van den Bergh S., Cohen J. G. and Crabbe C. 2001, AJ, 121, 611
- Zabludoff A. I., & Mulchaey J. S. 1998, ApJ, 496, 39
- Zeldovich Y. B., 1970, A&A, 5, 84